Accepted Manuscript

Influence of the initial cooling rate from γ′ supersolvus temperatures on microstructure and phase compositions in a nickel superalloy

Muzi Li, James Coakley, Dieter Isheim, Gaofeng Tian, Barbara Shollock

PII: S0925-8388(17)33699-X

DOI: 10.1016/j.jallcom.2017.10.263

Reference: JALCOM 43660

To appear in: *Journal of Alloys and Compounds*

Received Date: 5 September 2017

Revised Date: 25 October 2017

Accepted Date: 28 October 2017

Please cite this article as: M. Li, J. Coakley, D. Isheim, G. Tian, B. Shollock, Influence of the initial cooling rate from γ′ supersolvus temperatures on microstructure and phase compositions in a nickel superalloy, *Journal of Alloys and Compounds* (2017), doi: 10.1016/j.jallcom.2017.10.263.

Influence of the initial cooling rate from γ' supersolvus temperatures on microstructure and phase compositions in a nickel superalloy

Muzi Li[1], James Coakley[2,3], Dieter Isheim[2,4], Gaofeng Tian[5], and Barbara Shollock[6]

[1]*Department of Materials, Imperial College London, London, United Kingdom, SW7 2AZ,* (*E-mail: muzi.li13@imperial.ac.uk*)

[2]*Department of Materials Science and Engineering, Northwestern University, Evanston, Illinois, USA, 60208*

[3]*Department of Materials Science and Metallurgy, University of Cambridge, Cambridge, United Kingdom, CB3 0FS*

[4]*Northwestern University Center for Atom-Probe Tomography (NUCAPT), 2220 Campus Drive, Evanston, Illinois, USA, 60208*

[5]*Aeronautical institute Materials Beijing, AVIC, Beijing, P. R. China, 100095*

[6]*International Digital Laboratory, WMG, University of Warwick, Coventry, United Kingdom, CV4 7AL*

Abstract

Different cooling paths from a supersolvus temperature have been applied to FGH96, a polycrystalline nickel base superalloy for turbine disc applications, in order to simulate the different microstructures that exist through the thickness of a disc following an industrial heat treatment. Secondary and tertiary γ' precipitate size distributions and morphology have been analysed and compared for the different heat treatments using SEM and atom probe tomography (APT). Detailed compositional data for both γ' precipitate and γ matrix are presented, and compared to equilibrium compositions calculated by Thermo-Calc. For the heat-treatments studied, the secondary γ' composition indicates a shell of differing composition to that towards the precipitate core. From sequential equilibria compositional calculations, it is suggested that the 'shell' forms at a lower temperature than the precipitate core. The fine tertiary precipitates do not show the core-shell compositional differences on continuous cooling. W peaks are noted at the γ/γ' interfacial region, which is of significance for retarding coarsening. A γ' depletion zone surrounds the secondary precipitates, within which the γ matrix composition differs significantly to the γ far-field values, Finally, a precipitate nucleation and growth mechanistic model is suggested based on the experimental data and Thermo-Calc calculations.

Keywords: Nickel base superalloy, γ/γ' composition, Atom Probe Tomography, Particle size distribution, Nucleation and growth.

1 Introduction

Nickel base superalloys are extensively used in elevated temperature environments such as gas turbines due to their excellent strength, ductility, fatigue resistance and oxidation resistance at elevated temperature [1]. The good mechanical properties of such alloys are derived from their internal structure: a combination of a FCC γ matrix and a coherent $L1_2$ γ' precipitate which inhibits dislocation motion effectively, especially at relatively high temperature. FGH96 is a second generation poly-crystalline turbine disc material fabricated by a powder metallurgy route that was developed for improved creep strength and lower fatigue crack growth rate compared to the previous generation FGH95 (René 95). Its highest service temperature is reported as 750°C [2]. The nominal chemical composition of this alloy in wt.% is: 2.1% Al, 12.9% Co, 15.7% Cr, 3.7% Ti, 4% Mo, 4% W, 0.7% Nb, 0.05% Zr, 0.05% C, 0.03% B and balanced Ni. The elements and composition are carefully tailored in order to obtain the required properties in nickel base superalloys. For example, Al and Ti promote γ' precipitate formation, the combined amount decides γ' volume fraction; Cr provides excellent corrosion resistance; Co lowers the stacking fault energy; W improves the strength of the γ matrix, while Mo and Cr form carbides and borides with B and C and segregate to grain boundaries [3, 4].

It has been found that the microstructure of these alloys, especially in terms of γ' precipitate size distribution, morphology and chemical compositions, significantly affects the materials' mechanical properties [5-9], which can be altered significantly by heat treatment. This is due to the ease with which dislocations can cut through and/or bow around the precipitates. The lattice mismatch between γ and γ' phase depends on their composition and γ' precipitate size and therefore element partitioning and precipitate size have an essential impact on dislocation

movement while deforming. Generally speaking, the stress necessary for dislocations to bow around the precipitates is inversely proportional to the inter particle distance, and this distance increases with particle size. The FGH96 alloy is typically subjected to a two stage heat treatment. The first stage includes solutionising the material at a temperature above the solvus temparature, usually at 1150°C, for 30 to 60 minutes to dissolve all the γ' phase. This includes dissolution of the large primary γ' precipitates located at γ grain boundaries, such that the grains can grow. This is followed by continuous cooling to room temperature at appropriate cooling rates, to form secondary and tertiary γ' precipitates (also known as cooling γ' together) within grains. The second stage involves ageing the material at a certain temperature (usually 760°C) to refine the dispersion of the γ'. The tertiary γ' has near spherical shape and is much smaller in size than secondary γ' precipitates.

In superalloys such as FGH96, the γ' precipitate size distribution and morphology strongly depends on the applied cooling rate. When cooling rate is rapid, such as water quenching the alloy from a supersolvus temperature, a monomodal size distribution of fine γ' precipitates is obtained [10-13]. These precipitates are nanoscale in size with near spherical morphology and their number density is rather high. In industrial applications, however, such fast cooling rates are not usually applied because the thermal stresses induced by the quenching process can sometimes exceed the ultimate strength of the alloy, resulting in crack formation [14]. Slower cooling rates are generally applied in order to obtain a bimodal size distribution of γ' precipitates [10, 12, 15-18]. Multimodal size distribution are generally attributed to multiple distinct bursts of nucleation of precipitates at different undercoolings below the γ' solvus temperature [16]. These multiple nucleation bursts in turn result from the complex interplay of: (i) continuously increasing thermodynamic driving force for nucleation (chemical free energy difference) due to

increasing undercooling; (ii) a reduction in this driving force due to previous nucleation events; and (iii) the rapidly declining diffusivity of alloying elements with decreasing temperature [16]. However, due to the relatively large scale of turbine disc (about 40mm in thickness at the rim [19]) and the poor thermal conductivity for a series of cast superalloys (~10 W/(mK) [20]), compared to aluminium (~200 W/(mK)) and copper (~380 W/(mK)) at room temperature [21], it is challenging to maintain a uniform cooling rate across the whole disc. When subject to oil quenching from a single γ phase solid solution above the solvus temperature (a typical industrial heat treatment for FGH96), layers of different γ' size distribution can form across the thickness direction due to uneven cooling rates [22]. The disc surface is exposed to cold oil directly and therefore has narrow γ' particle size distribution with small γ' size due to high undercooling. At the central region, the undercooling is low and therefore has a coarse γ' distribution. Many researches revealed that coarser γ' distributions generally have weaker creep strength due to larger inter-particle distance which requires less energy for dislocation motion [23-26]. This unevenness of γ' distribution across the disc could cause strain localisation and thus decrease the creep life of the component. Thus it is important to understand the mechanism of the microstructural change in terms of size distribution, morphology and chemical composition.

Three-dimensional microstructural characterisation of nickel base superalloys at atomic scale via 3D atom probe tomography (APT) has been employed over the years [4, 13, 27]. The most recent atom probe system, local electrode atom probes (LEAP®) incorporating a local electrode in close proximity to the specimen was first commercially introduced by Kelly et al. in 2003 [28]. Compared to the more traditional atom probe field ion microscopy, LEAP provides not only faster data acquisition and lower voltages due to the local electrode but also substantially larger field-of-view (FOV) over which high mass resolution can be achieved, which leads to data

generation from larger volumes over the same time period [29, 30]. In modern atom probe equipment such as CAMECA's LEAP 3000X^{TM} and LEAP 4000X^{TM}, laser pulsing is used to assist generating pulsed field evaporation so that it produces a very low energy spread from the ions, which results in very high mass resolving power (MRP) for long flight times compared to voltage pulsing [29]. Recently, several studies have been conducted on both binary Ni-Al alloy and commercial superalloys [11, 31-36] via APT. These studies primarily focused on the changing of γ/γ' compositions during isothermal annealing after fast and/or slow quenching from the high temperature single γ phase resulting in a either monomodal or bimodal γ' distribution. Although these studies are informative in understanding element partitioning as well as γ' nucleation and growth, the applied heat treatments are quite different from industrial situations. Therefore, the current paper focuses on the size distribution, morphology and composition of secondary and tertiary γ' precipitates generated from different cooling rates throughout the disc as well as the compositional partitioning between these γ' precipitates and the adjacent γ matrix. APT provides detailed chemical analysis at the nanoscale, but is not suitable for analysing coarse γ' precipitates morphology and distribution. SEM (Scanning Electron Microscopy) is a more suitable technique for better understanding of an overall coarse γ' size distribution and morphological features over a larger scale. The three primary objectives of this paper are as follows:

1. to analyse γ' size distribution and morphology change corresponding to different heat treatments applied to FGH96 samples as well as the γ' particle number density via SEM and APT;
2. to understand the compositional difference between different generations of γ' and the relationships with cooling rate as well as the near-field (in the vicinity of a precipitate)

and far-field (not in the vicinity of a precipitate) γ phase compositions carried out by APT analysis;

3. to understand and illustrate the mechanism for γ' nucleation and growth and the elemental diffusion behaviour upon cooling.

2 Experimental

The FGH96 material was provided by BIAM (Beijing Institute of Aeronautical Materials Co., AVIC). The FGH96 alloy in this study has a composition of 2.1% Al, 12.9% Co, 15.7% Cr, 3.7% Ti, 4% Mo, 4% W, 0.7% Nb and balance Ni in weight percentage or 4.6% Al, 12.9% Co, 17.8% Cr, 4.5% Ti, 2.5% Mo, 1.3% W, 0.44% Nb and balance Ni in atomic percentage. The samples were cut from a disc by electro discharge machining in a tangential direction, which is the force direction on turbine discs during service. A supersolvus solutioning temperature of 1150°C was applied for 40min to the samples, then individual samples were cooled at different continuous cooling rates of 25, 50, 100 and 150°C/min to room temperature in order to simulate different undercoolings throughout the disc in the thickness direction. The sample names in this paper are referred to as F25, F50, F100 and F150 respectively. For comparison, another sample was cooled at the rate of 25°C/min to 1050°C followed by 150°C/min to room temperature which is referred to as IC (interrupted cooling). All samples were subsequently aged at 760°C for 8 hours followed by air cooling.

For SEM analysis, the samples were mechanically ground and polished then electro-etched with an etchant solution consisted of 35ml H_3PO_4, 2ml H_2SO_4 and 3g CrO_3 and an applied voltage of 2.5 - 3V for 1-2 seconds. SEM imaging was performed on a LEO GEMINI 1525 field emission scanning electron microscope. ImageJ software was applied for digital analysis, in which the secondary γ' average size, particle size distribution, particle number density and roundness were determined. For representative statistics, at least 200 particles were counted from each micrograph, and three micrographs taken from different grains were analysed. The errors for image analysis in this study are taken as 95% confidence derived from statistical treatments.

Samples for APT analysis were cut to 0.5mm×0.5mm×10mm match sticks with a slow speed cutting blade and electro-polished to a needle shape with tip diameter less than 100nm. The electro-polishing contained two steps: In the first step, the samples were immersed in an etchant of 25 vol.% $HClO_4$ in butoxyenthanol at 20V (DC) for coarse polishing; Fine polishing for the second step was performed using a solution of 2 vol.% $HClO_4$ in butoxyethanol at 7V. A LEAP 4000X Si instrument, located at the Department of Materials Science and Engineering, Northwestern University was used to carry out the APT experiments. APT measurements were carried out in the UV laser assisted field evaporation mode at a wavelength of 355nm, with an evaporation rate of 0.3 to 1.0%, a laser pulse repetition frequency of 500 kHz, laser pulse energy from 18 to 45pJ and a tip base temperature of 40K. IVAS 3.6 software was used for data analysis. Approximately 36 to 270 million atoms were collected for each APT sample. Mass spectrums of these samples were obtained after data collection, enabling the elements Al, Cr, Co, Ti, Ni, Mo, W, Nb, and Zr, C, B to be isolated.

3 Results

3.1 γ' size distribution and morphology

Fig. 1 shows the SEM images of the FGH96 samples that underwent different cooling paths. Cooling from a supersolvus temperature results in a bimodal γ' distribution. Two categories can be defined based on average size, morphology, and number density: secondary γ' precipitates with a relatively large size, irregular shape and low number density; and tertiary γ' precipitates with a small size, spherical shape and high number density. The secondary γ' precipitates are evenly distributed in the γ matrix with the tertiary γ' precipitates present in the γ matrix are separated by secondary γ'. For the continuous cooling samples, Fig. 1a – d, the secondary γ' size decreases with increasing cooling rate due to higher undercooling which restrains elemental diffusion rate; and its morphology changes from a butterfly-like shape to near spherical. The detailed statistics analysed from ImageJ software are listed in Table 1. The mean-equivalent diameters were calculated from the areas of the precipitates which were treated as equivalent circles. The roundness is used to evaluate the precipitate morphology, the closer this value is to 1, the closer the precipitate is to spherical. For a perfect circle, the roundness value is 1, for a square it is 0.75. As the results suggest in Table 1, the roundness values of the secondary γ' precipitates increase with cooling rate for the continuously cooled samples. Due to a high nucleation driving force resulting from high undercooling, the particle number density for secondary γ' precipitates increases with cooling rate, and the average inter-particle distance decreases. For IC (Fig. 1e), due to the 2-stage cooling path, the average γ' sizes of both secondary and tertiary are in the middle range with respect to continuous cooling. The

quantification of tertiary γ', however, is at the limit of SEM, and is also subject to error from etching effects and binary image processing. Indeed, quantification by TEM was not attempted as accurate quantification of the tertiary particle is hindered by the fine particle size relative to foil thickness, and this methodology also requires binary image processing.

The secondary γ' particle size distribution (PSD) is shown in Fig. 2. It shows that for a slow cooling rate, the range of secondary γ' precipitate diameter (about 40 – 480 nm for F25) is wider than that of the fast cooling rate (about 40 to 180 nm for F150), indicating that the nucleation events of secondary precipitates in the more slowly cooled sample occurred over a broader temperature range and also that the higher cooling rate restricted precipitate growth, leading to a narrower size distribution.

The tertiary γ' precipitates (not presented in the PSD) are nucleated at higher undercooling due to the super-saturation of γ' favoured elements (Al and Ti) provides a high thermodynamic driving force but the growth rate is limited due to a lower diffusivity rate at lower temperatures.

3.2 Chemical composition analysis of γ' phase

3.2.1 Continuous cooling

The chemical composition analysis for both γ and γ' phases have been conducted using atom probe tomography. The 3D reconstruction of F25 with 80 million atoms counted in total is shown in Fig. 3a. An iso-concentration surface value of 12 at.% Al+Ti, shown in red, has been applied to differentiate the γ and γ' phases (a phase containing more than 12 at.% Al+Ti is considered as γ', and γ otherwise). A background level of 5% Ni ions is shown in blue to highlight the geometry of the sample needles. A secondary γ' precipitate is observed at the top left region of the needle, surrounded by a tertiary γ' depleted zone. The tertiary γ' in the vicinity

of the depleted zone are smaller in size than those away from the depleted zone. Fig. 3b shows the 3D reconstruction of F150 with a total of 270 million atoms counted. Again, both secondary and tertiary γ' precipitates are presented with an isoconcentration surface value of 12% Al+Ti shown in red, and a tertiary γ' depletion zone is observed around the secondary γ' precipitates. The tertiary γ' precipitates are again smaller close to the depletion zone and larger away from it. The size of tertiary γ' was deduced from the APT data using an ion count method. Using the 12% Al+Ti isoconcentration surface value, there is a slight decrease in mean size from approximately 12 to 9 nm ± 1nm for the continuous cooled samples, however, these nano particle size quantified by APT is dependent on the isosurface value applied.

Fig. 4 illustrates proximity histogram concentration profiles (proxigrams for short) across the γ/γ' interfaces of the main alloying elements in FGH96 (Cr, Al, Co and Ti). The proxigrams represent three different continuous cooling rates, and were constructed using the Al+Ti = 12 at.% isoconcentration surface value and a bin size of 0.1nm. The proxigrams clearly reveal that the γ phase (represented as negative x values of each plot) is enriched in Cr and Co and depleted in Al and Ti, with the γ' phase (positive x values of each plot) showing the opposite. The compositional data in these proxigrams were averaged from the detected γ' precipitates: 3-6 precipitates for secondary γ' and 50-200 for tertiary γ'. Although the tertiary γ' precipitate size varied within an APT specimen, depending on its proximity to a secondary precipitate, a compositional variation due to this size difference was not found.

Compositional gradients of Al and Ti are observed within the secondary γ' precipitates, highlighted by black arrows in Fig. 4a, c and e, but are not observed within the tertiary γ' precipitates, Fig. 4b, d, e. These composition gradients show that the Al concentration in the secondary γ' decreases from the interface towards the core of the particle while that of Ti

increases. No correlation has been found between cooling rate and these gradient changes for Al or Ti. The compositional gradient can be rationalised by considering that the shell of the secondary precipitate nucleated at a lower temperature than the core, and the diffusion rates are then too low to achieve uniform compositional equilibrium at low temperatures within the precipitate. Table 2 shows the γ' compositions for samples F25, F50, F100 and F150, along with 760°C equilibrium composition calculated by Thermo-Calc software and the TCNI5 database. 760°C equilibrium composition is displayed in the table is because the samples were subsequently aged at 760°C. For each cooling rate, there are 3 categories: secondary-shell (calculated from 5-7nm away from the γ/γ' interface centre into the precipitate in each proxigram), secondary-toward-centre (calculated from 30-35nm away from the γ/γ' interface centre into the precipitate in each proxigram) and tertiary γ' composition. The errors are not plotted as they obscure the data, but are less than 1% of the data. The correlation between cooling rate and secondary-toward-centre γ' composition has been found to be minimal. Only the Cr and Co concentrations tend to increase with a higher cooling rate. A possible reason could be a factor of 6 (150°C/min / 25 °C/min) difference in the cooling rate may not have been sufficient to observe a difference in the chemical ordering of secondary γ' precipitates that occurs, and a much higher cooling rate would be required to observe any difference. Indeed, Singh [15] compared the composition of secondary γ' when water quenched (>300°C/min) and slow cooled (24°C/min), and the results clearly showed a difference in the γ' composition of these two samples.

For the tertiary γ' compositions, there is no clear evidence of compositional difference in the range of cooling rates in the present study, this could be associated with the post 8h ageing at 760°C resulting in diffusion and diminishing the compositional difference for different cooling

rates. The last column of Table 2 is the combined concentration of Al and Ti. It shows that Al+Ti content is similar for the γ' phase (secondary-toward-centre, secondary-shell and tertiary γ') for the same heat treatment. A detailed analysis is conducted in section 4.2.

Fig. 5 shows the proxigrams of F25 and F150 for low content elements Mo, W and Nb. It can be seen that the γ phase is enriched in Mo and γ' is enriched in Nb. Like Al, Nb also exhibits a declining concentration away from the interface in the secondary γ' precipitates (see arrows), and this is not observed in the tertiary γ' precipitates. W exhibits a unique partitioning behaviour: Clear W peaks have been found at the γ/γ' interfaces for both secondary and tertiary γ' as shown in Fig. 5. The 760°C equilibrium composition of γ' (Table 2) and γ phases (Table 4) calculated by Thermo-Calc suggest that W tends to segregate to the γ phase. The γ' phase ejects W to the γ phase upon cooling, but due to the large atomic radius of W (W: 0.193nm, Ni: 0.149nm, Al: 0.118nm), its diffusivity is relatively slow, and therefore a peak of W is formed at the interface and its composition decreases towards the γ' phase centre. This is reasonable as W is deliberately added to nickel-base superalloys such as FGH96 to slow down diffusion and retard coarsening at high temperature. The enrichment of W at the γ/γ' interfaces has also been found in other commercial nickel-base superalloys analysed by APT [37]. The W enrichment at the interface is lowered with higher diffusion rates and/ or time. This is seen in Fig. 5, where the W enrichment at the interface of secondary γ' in F25 is not as sharp as that of sample F150.

3.2.2 Interrupted cooling

The 3D reconstruction image from the sample IC is shown in Fig. 6, it indicates that unlike the continuous cooled samples, the interrupted cooling path created 3 distinctive γ' populations: secondary γ', large tertiary γ' and fine tertiary γ'. The proxigrams of these three γ' types are

shown in Fig. 7. The Al concentration decreases in secondary γ' away from interface, while Ti increases (Fig. 7a) in the same way as for the continuously cooled samples (Fig. 4). Again, this trend for Ti and Al concentration was not found in the fine tertiary γ' (Fig. 7e). The compositional change of Al and Ti for large tertiary γ', however, shows similar trend for the Al and Ti compositions to the secondary γ' precipitates but the absolute values of the composition gradients are not as large. This is evident as a convergence of the Al and Ti concentration profiles in secondary γ' (arrowed in black) while those of large tertiary γ' do not converge as shown in Fig. 7c. The large tertiary γ' precipitates have characteristics between secondary and tertiary γ' in terms of size and chemical compositions (based on the APT results). The data shown in Table 3 is evidence of this phenomenon. Like the continuously cooled samples, the secondary-shell composition is somewhere between secondary-toward-centre and tertiary. For the large tertiary γ', the shell composition is close to tertiary γ', but the centre is closer to secondary-toward-centre. The Mo and Nb participation behaviours are similar with continuous cooled samples. W peaks are also present at the γ/γ' interface for both secondary and tertiary precipitates.

3.3 Chemical composition analysis of γ phase

Not only have compositional differences in γ' been found, the γ phase near these precipitates also exhibits local compositional variations. Composition gradients from the γ phase towards the γ/γ' interface of the plotted 4 elements have been observed (Fig. 4, arrowed in red), in which the Cr and Co exhibit positive gradient slope values (concentrations increase towards the interface) while Al and Ti exhibit negative values (concentrations decrease towards the interface). When comparing between cooling rates, the gradients increase with cooling rate. For the same cooling

rate, when comparing compositional gradients in the γ phase originating from secondary and tertiary γ' precipitates, no difference is found for F25 and F50 (slow cooling), but for F100 and F150, the compositional gradients within γ are greater from the γ to tertiary γ' precipitates than from the γ phase to secondary γ'.

Fig. 8 shows magnified proxigrams for Cr, Al and Ti in the γ matrix of F25 and F150 from the γ phase on the left of the plots to the γ/γ' interface on the right of the plots, thus highlighting the precipitate free depletion zone of the γ near the interface. Both near-field and far-field (up to -35nm) matrix compositions are presented in the plots. As can be seen from Fig. 8(a), for both F25 and F150, the Cr compositions near the interface are much greater than away from the interface. Compositional variations moving away from the interface in the γ phase are also observed in Al and Ti (Fig. 8b). The γ matrix is depleted in Al and Ti for both F25 and F150 next to the interface, with composition of ~1 at.% and ~0.5 at.% respectively. The Al and Ti compositions increase gradually away from the interface. These observations are supported by the data in Table 4, in which the γ compositions for each sample have been listed based on 3 categories: γ near secondary γ' precipitates (-7 to -5nm from the centre of the interface), γ far from secondary precipitates (-33 to -30nm from the centre of the interface) and γ near tertiary precipitates (-7 to -5nm from the centre of the interface).

When comparing the far-field γ composition from different cooling rates, it is clear that the decrease of Cr composition and increase in Al and Ti compositions away from the interface and into the matrix is more dramatic for F150 than for F25, as is shown in Fig. 8. This is associated with the higher undercooling that limits diffusion in the more rapid cooled sample (F150). Table 4 shows the compositional changes in detail. Slow cooling rates (F25 and F50) exhibit more Cr

and Co content and less Al and Ti in the far-field γ composition compared to fast cooling (F100 and F150), indicating that a higher undercooling limits elemental diffusion rate.

4 Discussion

4.1 γ' precipitation mechanism upon cooling and subsequent ageing

Based on the detailed compositional analysis of γ and γ' phases from APT experiments and the size and morphology analysis from SEM images, a mechanistic model can be proposed to explain the overall γ' precipitation process upon cooling and subsequent ageing for the FGH96 superalloy. When cooling from a supersolvus temperature, the chemical volume free energy, ΔG_v, continues to increase with increasing undercooling once the temperature is below solvus (1120°C for FGH96), until the critical activation energy barrier ΔG^* for nucleation is low enough to be overcome, leading to the first burst of nucleation. In the case of the slow cooled sample F25, a slow cooling rate results in precipitation occurring at relatively high temperature where diffusion rates are relatively fast. This promotes rapid elemental partitioning between the secondary γ' precipitates and the surrounding γ matrix; that is, Al and Ti partition to the ordered γ' phase while Cr and Co partition to γ phase. These secondary γ' precipitates grow rapidly due to fast elemental partitioning, and the precipitate morphology develops from spherical shape to cuboidal or butterfly shape once the anisotropic elastic strain energy surpasses the isotropic interfacial energy. Meanwhile, the driving force for nucleation is relatively low under low undercooling which results in a low particle number density ($8/\mu m^2$, Table 1), and the precipitates are separated by large distances (average particle distance of 157nm, Table 1).

In the applied heat-treatment of sample F25, the near filed γ phase at the γ/γ' interface of the secondary precipitate is depleted in Al and Ti while enriched in Cr and Co forming γ'-free depletion zones around the secondary γ'. These precipitates are enriched in Al and Ti whereas

depleted in Cr and Co (composition data in Table 2 and Table 4). However, long-range γ equilibrium was not achieved following cooling and subsequent ageing, resulting in a compositional gradient through the γ matrix (Fig. 8). During the continuous cooling, new nuclei form with continuous nucleation driving force building up from increased undercooling, which produces a broad γ' size distribution (Fig. 2). As secondary γ' precipitates grow in size during initial cooling, when the long range diffusion fields of two adjacent precipitates overlap (often referred to as soft impingement) [17], it is more energetically favourable for precipitate growth instead of new secondary γ' nucleation within γ between these precipitates. One would assume that not until the γ' forming elements Al and Ti in the far-field γ phase are super-saturated and the undercooling temperature is low enough with a critical energy barrier ΔG^* sufficiently low, does a second burst of nucleation occur, forming tertiary γ' precipitates in the γ phase between secondary γ' precipitates, next to depletion zones, consuming part of the built nucleation driving force as well as eliminating elemental super-saturation. These tertiary γ' precipitates are very small in size and high in number density due to limited diffusivity of atoms under such high undercooling coupled with a great thermodynamic driving force for nucleation. Also, they are relatively smaller in size close to the depletion zones and larger away from these zones (Fig. 3), presumably because the driving force for nucleation in the γ matrix is higher away from the depletion zone (higher Al content and lower Cr away from the depletion zone). The growth of secondary γ' continues during tertiary γ' formation and during ageing, and a 'shell' of different composition to the core is deposited on the secondary γ' precipitates (Table 2). This 'shell' composition is somewhere between that of secondary and tertiary γ'.

For the fast cooled sample F150, when it's cooled from the same supersolvus temperature and aged subsequently, due to higher undercooling and reduced atom diffusivity coupled with a high

nucleation driving force, the secondary γ' precipitates are high in number density (42/μm^2, Table 1), small in size, remain near-spherical shape (Fig. 1 and roundness value in Table 1) and possesses narrow particle size distribution (Fig. 2). The basic mechanisms for both secondary and tertiary γ' formation are very similar with F25. The final composition of secondary γ' lies further away from the calculated 760°C equilibrium compared to F25 due to the faster cooling rate, as evidenced by more Cr and Co towards the core of the secondary γ' in Table 2, although this difference is very subtle. Also, due to the high number density of secondary γ' in F150, the distance between these secondary precipitates are narrower (67nm average particle distance in Table 1), so that the tertiary γ' size difference near and away from the precipitate depletion zones isn't as apparent as in F25 (Fig. 3). No clear relationship has been found between the tertiary γ' compositions and the cooling rate (Table 2), which may indicate that tertiary γ' precipitates were formed over a relatively short temperature range. Singh et al. [16] studied the γ' nucleation and growth in Rene 88DT alloy, which is a very similar alloy to FGH96, and found that at a cooling rate of 24°C /min, the tertiary γ' nucleate between ~800 and 700°C.

For F50 and F100, these two samples also exhibit bi-modal γ' distribution and the γ' growth mechanism is similar with F25 and F150. The secondary γ' precipitates again show compositional variation from the precipitate core towards the 'shell', with the 'shell' composition close to that of the tertiary γ' precipitates.

Finally, for sample IC, the interrupted cooling path and subsequent ageing resulted in 3 γ' populations, with low secondary γ' particle density and a wide interparticle distance (Table 1). The γ' nuclei formed are as described for the F25. The change in cooling rate to from 25 to 150°C/min at 1050°C (in the temperature range corresponding to secondary γ' formation), limits the further diffusional growth of these secondary precipitates. A larger tertiary γ' nucleated as a

result of the interrupted cooling heat-treatment. These large tertiary precipitates are relatively larger in size as compared to the fine tertiary precipitates (Fig. 6). They also possess compositions that vary from the precipitate core to the shell (Table 3). The fine tertiary γ' are formed following the same mechanism as the continuous cooled samples (Table 3).

4.2 Sequential equilibria

Using the TCNI5 database, Thermo-Calc has been applied to calculate the equilibrium compositions of γ and γ' phases from 1120°C down to 500°C for every 5°C in order to see the equilibrium concentration change for the elements during cooling. Fig. 9 shows the Al and Ti sequential equilibria diagrams for the γ' phase. It illustrates that the Al and Ti curves are symmetrical, with decreasing temperature, the Al equilibrium concentration increases while that of Ti decreases. These calculations rationalise the Al and Ti compositional differences for secondary and tertiary γ' in Table 2 and the compositional gradients of Al and Ti in secondary γ' in Fig. 4 (black arrows). At high temperature when secondary γ' nucleates, the calculated equilibrium concentration difference for Ti and Al is relatively large, for example (Ti - Al) ≈ 2 at.% at 1000°C, but this difference is much smaller at the lower temperatures where tertiary γ' is formed, for example this value is ≈ 0.8 at.% at 700°C. In addition, the Al + Ti compositional value remains steady in the temperature range studied. The APT experimental data, Table 2 and Table 3 of Al and Ti (the γ' forming additions) show the same trend as the sequential equilibria calculations. The Ti concentration towards the core of the secondary precipitates is greater than the Al concentration, while the Al concentration of the tertiary precipitates is in fact greater than the Ti concentration. Furthermore, the previously discussed concentration gradients from within the secondary precipitate to the secondary precipitate shell agree with the trends of the calculated

equilibria. From the APT experimental data, the Al concentration increases towards the shell, while that of Ti decreases, see the proxigrams of Fig. 4 and 6 and the tabulated data in Table 2 and 3. This appears to suggest that the shell forms at a lower temperature to the precipitate core. It is noted in the sequential equilibria calculations that the Al and Ti curves have inflection points around 970°C that are also symmetrical, see Fig. 9. This temperature could be the point at which secondary γ' precipitates stop nucleating so that the nucleation driving force keeps building up and therefore affects the equilibrium composition. This would be in agreement with a previous study, the nucleation temperature range for secondary γ' in Rene 88DT is found to be from ~1200 to ~1000°C [16].

5 Conclusions

1. Different cooling paths from a supersolvus heat treatment temperature have been applied on FGH96, a commercial powder metallurgy nickel base superalloy for turbine disc applications. The SEM images and post digital software analysis show that with increasing cooling rate both the secondary and tertiary γ' average size decrease, the secondary γ' morphology changes from butterfly like to spherical, and the particle number density increases while average inter-particle distance decreases. A higher cooling rate leads to a narrower secondary γ' particle size distribution. The interrupted cooling sample (IC) has 3 distinct γ' populations observed from the APT reconstruction: secondary, large tertiary and fine tertiary γ'.
2. Based on the APT data reconstructions, γ' free depletion zones are found adjacent to secondary γ' precipitates in the γ matrix, and tertiary γ' precipitates are found to be smaller in size near these depletion zones and bigger away from these zones.
3. Analysis of the APT data shows that the γ' phase is enriched in Al, Ti, and Nb, while the γ phase is enriched in Cr, Co and Mo. The composition of the 'shell' of the secondary precipitates formed on cooling, differ from towards the core of the precipitates. This core-shell difference in composition was not observed for the fine tertiary γ'. There is no evidence that the different cooling rate has influence on secondary-shell and tertiary γ' compositions, although the post ageing treatment might affect their composition.
4. Tungsten concentration peaks are found at the γ/γ' interfaces, which is evidence of W retarding coarsening at high temperature.

5. The γ phase composition within the precipitate free zones differs from the far-field γ compositions, and is dependent on the cooling rates. These zones are enriched in Cr and depleted in Ti and Al.
6. A model rationalising the γ’ nucleation and growth mechanism has been proposed based on the experimental data and analysis.
7. The difference of Al and Ti compositions (the γ’ forming elements) within secondary and tertiary γ’ precipitates, and the compositional gradient of Al and Ti from the γ/γ’ interface towards the core of the secondary γ’ precipitates, are rationalised in light of a sequential equilibria analysis calculated in Thermo-Calc, with good agreement shown between calculation and experimental data.

Table 1. Statistical results of secondary and tertiary γ' extracted from SEM images.

Sample ID	*Secondary γ' diameter (nm)*	*Particle density (no./μm^2)*	*RN*	*Tertiary γ' diameter (nm)*	*Average particle distance (nm)*
F25	220	8	0.72	26	157
F50	171	14	0.74	16	116
F100	128	26	0.76	16	90
F150	101	42	0.78	13	67
IC	149	16	0.78	15	141

Table 2. Secondary γ' particle compositions (at.%) of continuous cooling samples, determined from APT proximity histogram concentrations at (i) 5-7nm away from the center of the γ/γ' interface, into the secondary precipitates, termed 'secondary-shell'; (ii) the center of the tertiary precipitates; and (iii) 30-35nm away from the center of the γ/γ' interface, into the secondary precipitates, termed 'secondary-towards-center'. The compositional equilibrium of γ' precipitate at 760^{o}C, is also presented, calculated from Thermo-Calc using the TCNI5 nickel-base superalloy database.

Sample	Location	Ni	Cr	Al	Co	Ti	Mo	Nb	W	Al+Ti
F25	Secondary-shell	70.6	1.2	11.6	4.4	9.4	0.8	0.6	1.2	21.0
	Tertiary	70.0	1.4	12.2	4.3	8.6	1.0	0.7	1.6	20.8
	Secondary-towards-centre	70.8	1.6	10.1	4.9	10.8	0.6	0.4	0.7	20.9
F50	Secondary-shell	69.4	1.3	11.6	4.8	10.4	0.7	0.6	1.0	22.0
	Tertiary	70.1	1.2	12.2	4.8	9.4	0.9	0.4	1.3	21.6
	Secondary-towards-centre	68.8	1.8	10.8	5.4	11.4	0.5	0.6	0.7	22.2
F100	Secondary-shell	70.3	1.4	10.9	4.6	10.6	0.7	0.4	0.9	21.5
	Tertiary	69.6	1.5	11.9	4.3	9.6	0.9	0.5	1.4	21.5

	Secondary-towards-centre	69.8	2.0	9.6	5.5	11.4	0.6	0.3	0.7	21
F150	Secondary-shell	70.7	1.3	11.3	4.5	9.8	0.7	0.5	1.1	21.1
	Tertiary	70.5	1.5	11.8	4.4	8.8	0.9	0.5	1.4	20.6
	Secondary-towards-centre	69.8	1.9	10.1	5.4	11.2	0.5	0.4	0.7	21.3
Eq at 760°C	FGH96	69.3	1.7	10.3	5.8	11.0	0.1	1.1	0.6	21.3

Table 3. γ' particle compositions (at.%) of the interrupted cooling sample, determined from APT proximity histogram concentrations. The compositions are determined under three distinct precipitate-size categories: secondary, large tertiary and fine tertiary, see Figure 6. Similar to Table 2, the secondary and large tertiary γ' precipitates are separated into the compositions within the precipitate shell and towards the precipitate core, with the 'large tertiary towards-centre' value determined 15-20nm away from the interface. The calculated compositional equilibrium of the γ' precipitate at 760°C from Thermo-Calc and the TCNI5 database is presented.

Sample	Location	Ni	Cr	Al	Co	Ti	Mo	Nb	W	Al+Ti
IC	Secondary-shell	70.6	1.4	11.1	4.5	10.2	0.7	0.5	1.0	21.3
	large tertiary-shell	71.2	1.3	11.4	4.2	9.3	0.8	0.5	1.2	20.7
	Fine tertiary	70.9	1.3	11.7	4.2	8.8	0.9	0.5	1.3	20.5
	large tertiary-towards-centre	70.9	1.4	11.0	4.2	10.4	0.6	0.5	1.0	21.4
	Secondary-towards-centre	69.6	2.0	10.0	5.7	11.6	0.5	0.4	0.7	21.6
Eq at 760°C	FGH96	69.3	1.7	10.3	5.8	11.0	0.1	1.1	0.6	21.3

Table 4. Compositions of γ matrix (at.%) determined from APT proximity histogram concentration profiles for samples with different cooling histories. The matrix compositions are calculated at three locations: near secondary, far from secondary and near tertiary γ' precipitates. Near secondary: 5 to 7nm from the interface centre, into the matrix; Far from sec: 33 to -30nm from the centre of the interface; Near tertiary: 5 to 7nm from the interface centre. The calculated compositional equilibrium of the γ phase at 760°C from Thermo-Calc and the TCNI5 database is presented.

		Ni	Cr	Al	Co	Ti	Mo	Nb	W
F25	Near secondary	47.4	28.0	1.0	18.0	0.4	3.1	0.1	1.6
	Far from sec	49.5	25.8	2.0	16.5	1.2	2.9	0.2	1.6
	Near tertiary	47.4	28.2	1.0	17.7	0.4	3.2	0.1	1.7
F50	Near secondary	46.6	28.6	1.0	18.4	0.4	3.1	0.1	1.6
	Far from sec	51.4	24.0	2.7	15.8	1.6	2.7	0.2	1.5
	Near tertiary	47.4	29.6	1.1	17.8	0.4	3.0	0.1	1.5
F100	Near secondary	46.8	28.5	1.1	18.2	0.4	3.0	0.1	1.6
	Far from sec	51.5	23.5	3.2	15.2	2.0	2.5	0.2	1.6
	Near tertiary	47.3	28.4	1.1	17.8	0.5	2.9	0.1	1.6
F150	Near secondary	46.9	28.5	1.1	18.1	0.4	2.9	0.1	1.6
	Far from sec	51.3	23.9	2.8	15.7	1.8	2.6	0.2	1.6
	Near tertiary	47.4	28.2	1.1	17.9	0.5	2.9	0.1	1.6
IC	Near secondary	46.9	29.7	1.0	18.3	0.5	3.0	0.1	1.6
	Far from sec	51.7	24.2	3.0	15.5	2.1	2.6	0.2	1.5
	Near tertiary	47.5	29.5	1.1	17.9	0.5	3.0	0.1	1.5
Eq at 760°C	FGH96	48.7	28.4	1.2	17.3	0.3	2.7	0.03	1.4

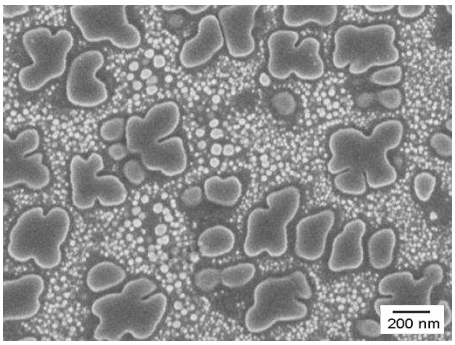

(a) F25 (25 ℃ /min)

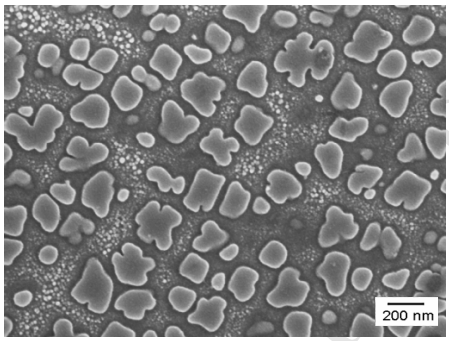

(b) F50 (50 ℃ /min)

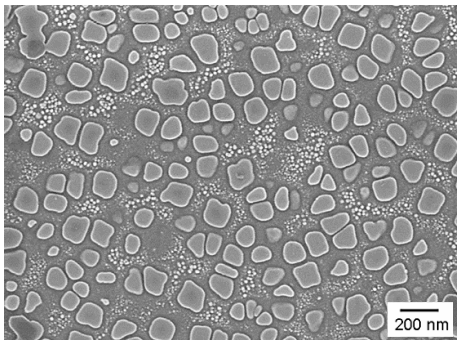

(c) F100 (100 ℃ /min)

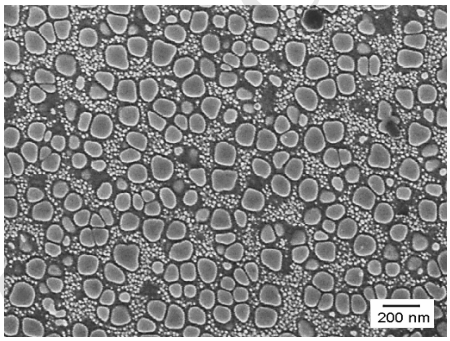

(d) F150 (150 ℃ /min)

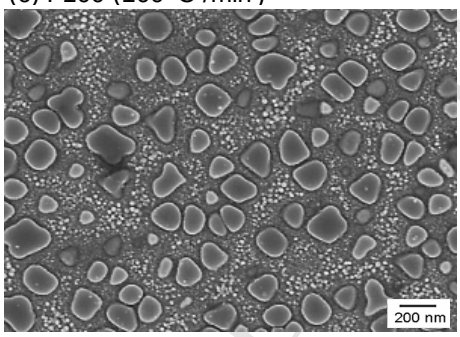

(e) IC (25 ℃/min to 1050℃ then 150 ℃/min)

Figure 1. SEM images showing the size and morphology of γ' precipitates after different heat treatments. All samples were cooled from a supersolvus temperature and have bimodal γ' distributions.

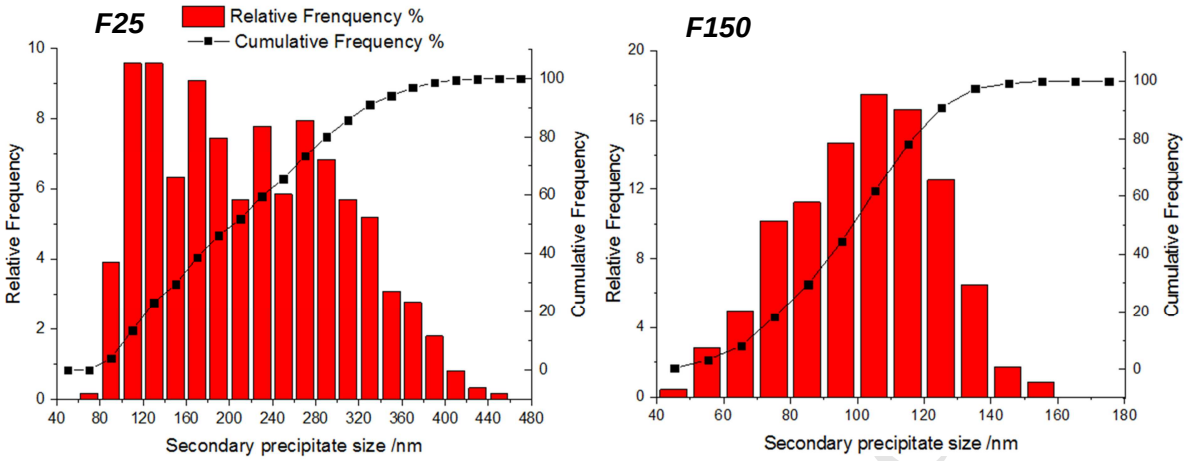

Figure 2. Secondary γ' precipitates size distribution of samples F25 and F150. A fast cooling rate leads to a narrower secondary γ' distribution.

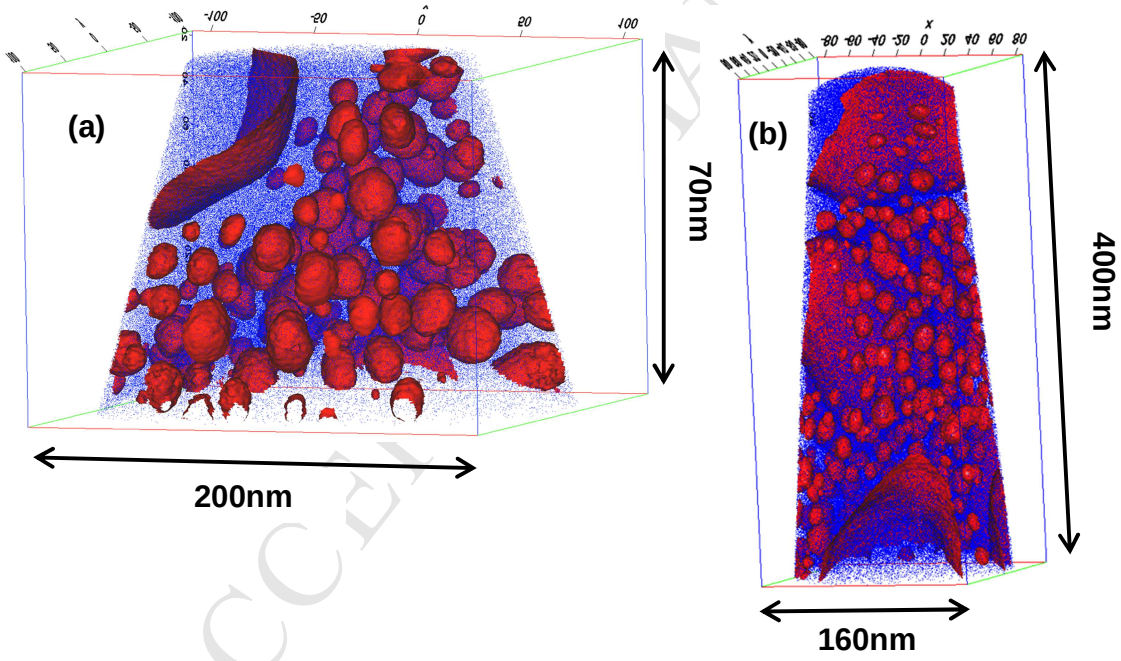

Figure 3. 3D APT reconstructions of sample F25 (a) with 80 million ions detected and F150 (b) with 270 million ions. The iso-concentration surface (or isosurface) value of 12 at.% Al + Ti is shown in red, both secondary and tertiary γ' precipitates can be seen clearly. 5% of Ni ions are shown in blue indicating sample geometry.

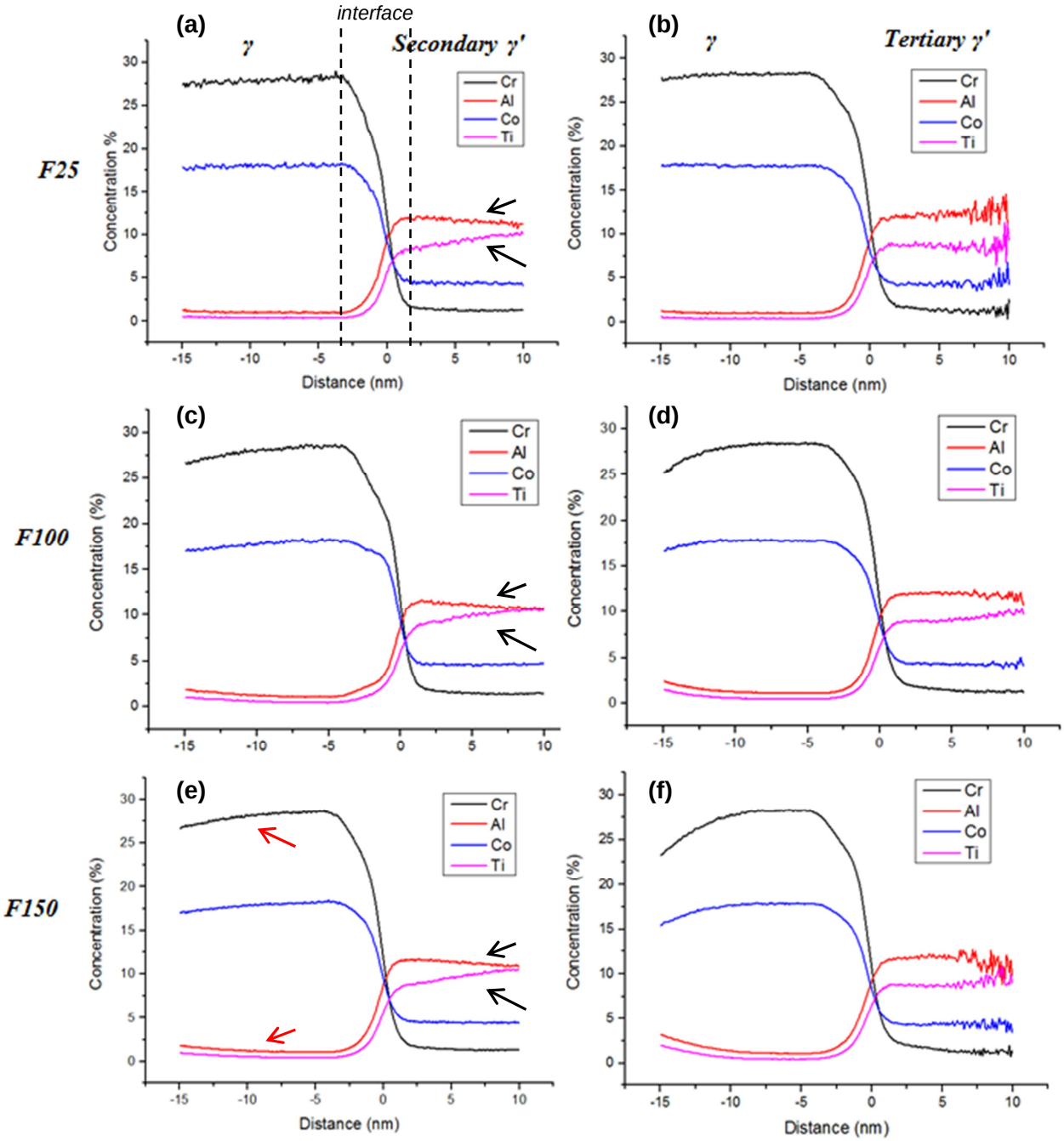

Figure 4. Proximity histogram concentration profiles (proxigrams) of the main elements in at.% (Cr, Al, Co and Ti) for F25, F100 and F150 across γ/γ' interface using an Al+Ti = 12% isoconcentration surface value. Left column proxigrams (a, c and e) show secondary γ' and γ interface and right column (b, d and f) shows tertiary. For all the proxigrams negative x values represent γ phase and positive x values represent γ'. The composition data in these proxigrams represent data from the detected precipitates, about 3-6 for secondary

and 50-200 for tertiary γ'. The black arrows highlight compositional gradients of Al and Ti within the secondary γ' precipitates. The red arrows highlight compositional gradients from the γ phase towards the γ/γ' interface.

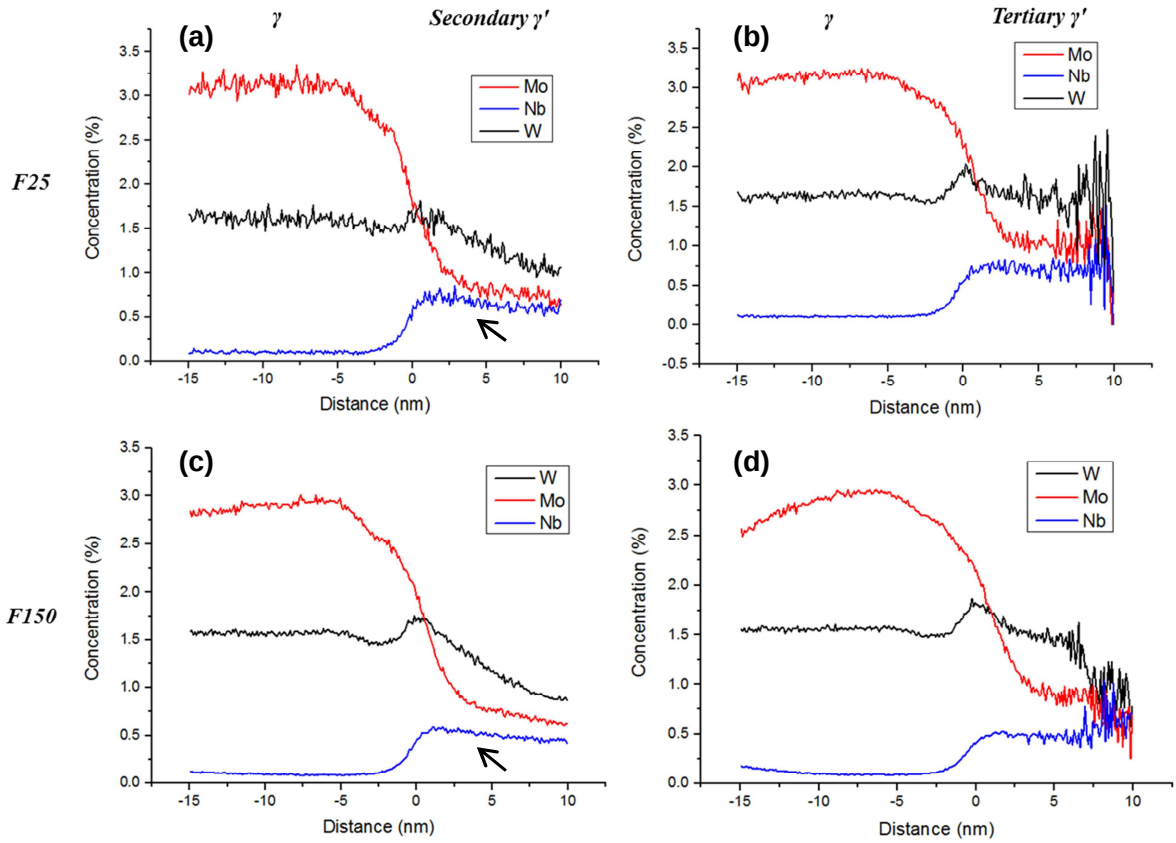

Figure 5. The proximity histogram concentration profiles (proxigrams) in at.% of Mo, W and Nb in samples F25 and F150 across the γ /γ' interface using Al+Ti = 12% isoconcentration surface values. The left column proxigrams (a and c) show the secondary γ' interface and the right column (b and d) shows tertiary. For all the proxigrams negative x values represent γ phase composition and positive x values represent γ'. The black arrows highlight compositional gradients of Nb within the secondary γ' precipitates, that are not observed in the tertiary γ' precipitates.

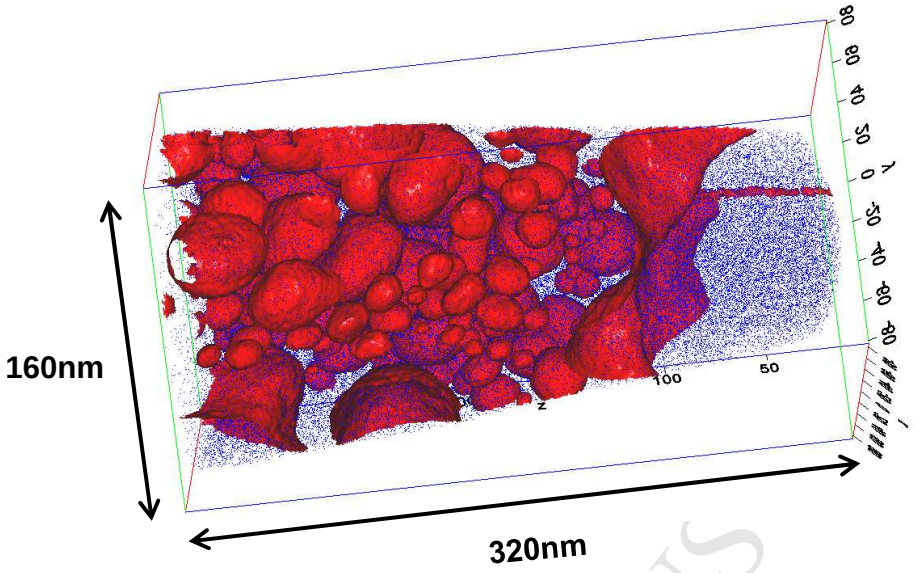

Figure 6. 3D APT reconstruction of sample IC with 208 million ions detected. The iso-concentration surface value of 12 at.% Al + Ti is shown in red, 5% Ni ions are shown in blue indicating sample geometry. 3 distinctive populations of γ' are observed: secondary on the right, large tertiaries on the left and fine tertiaries in the middle.

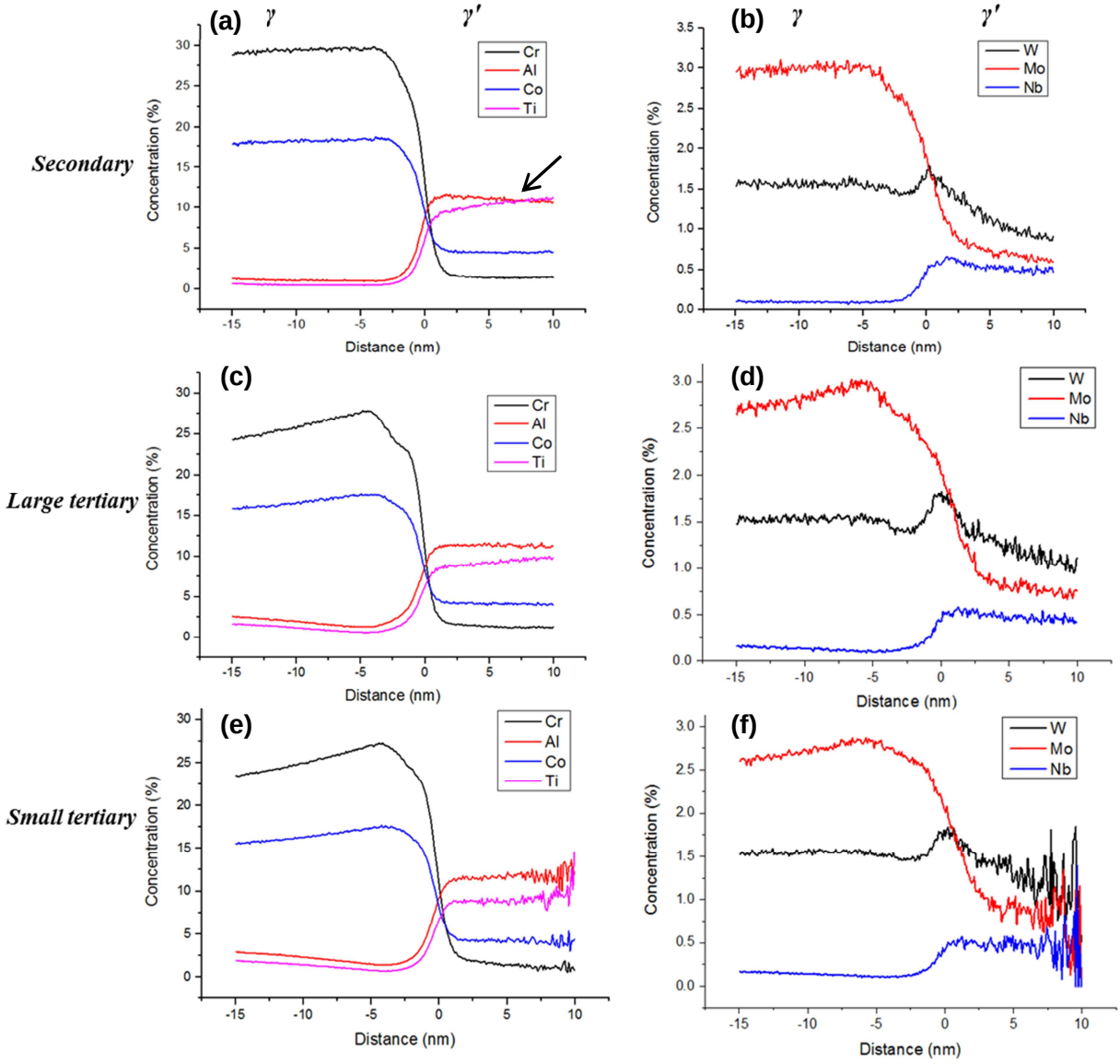

Figure 7. The proximity histogram concentration profiles in at.% of Mo, W and Nb in the IC sample across the γ /γ' interface using Al+Ti = 12% isoconcentration surface values. Left column proxigrams (a, c and e) show Cr, Al, Co and Ti and right column proxigrams (b, d and f) show Mo, Nb and W. For all the proxigrams negative x values represent γ phase composition and positive x values represent γ'. The black arrow highlights compositional gradients of Al and Ti within the secondary γ' precipitates. The large tertiary precipitates also exhibit this trend in Al and Ti, but not as dramatically.

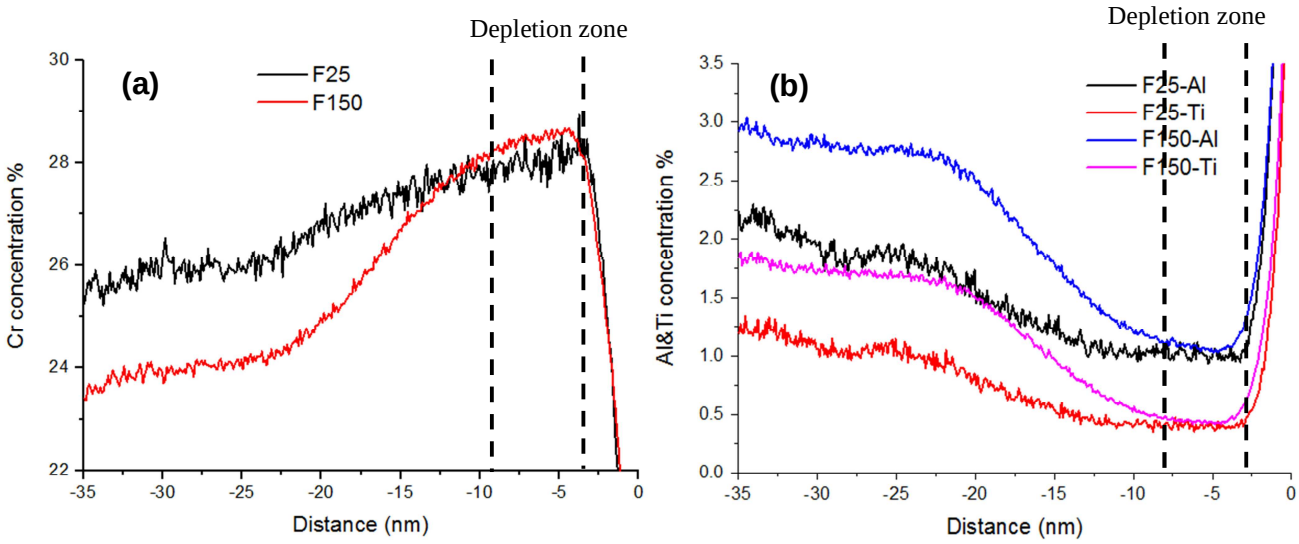

Figure 8. Magnified proximity histograms concentration profiles in at.% of the γ phase composition for F25 and F150 samples in the vicinity of secondary γ' precipitates. The plots show the near-field and far-field matrix composition of Cr (a), Al and Ti (b) in the γ matrix. The black dash lines represent depletion zones in γ phase.

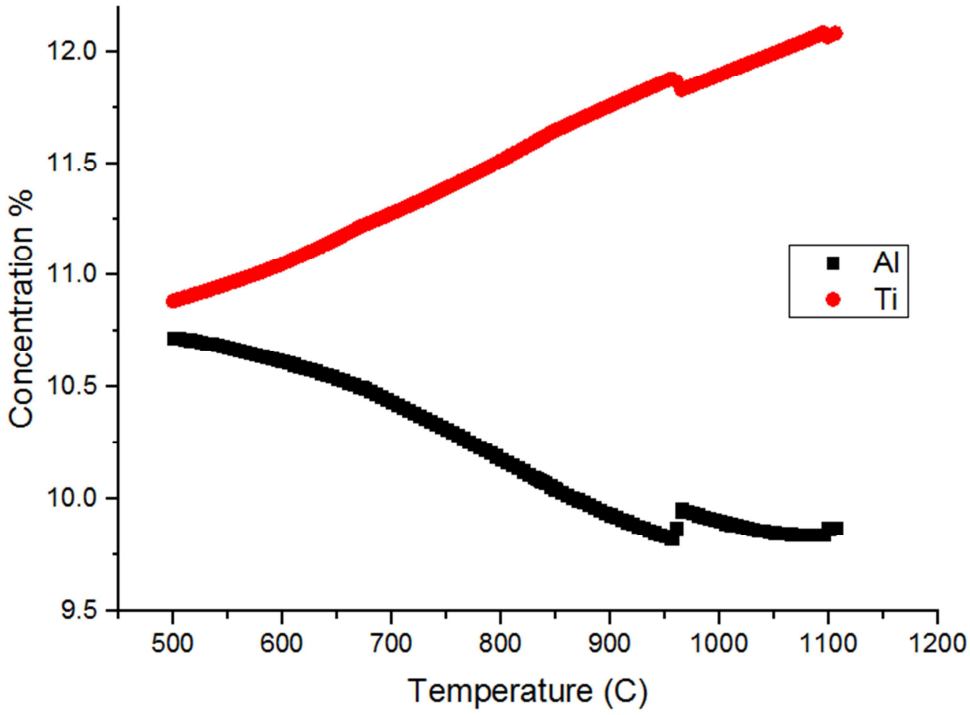

Figure 9. Sequential equilibria diagram of Al and Ti (at.%) in γ' phase from solvus temperature 1120°C to 500°C, calculated from Thermo-Calc and database TCNI5.

Acknowledgements

The authors are grateful to Beijing Institute of Aeronautical Materials Co., AVIC for the material used in this study and the financial support. Atom-probe tomography measurements were performed at the Northwestern University Center for Atom-Probe Tomography (NUCAPT) and the LEAP tomograph was purchased and upgraded with funding from the NSF-MRI (DMR 0420532) and ONR DURIP (N00014-0400798, N00014- 0610539, N00014-0910781) programs. NUCAPT is a Shared Facility of the Materials Research Center of the Northwestern University, supported by the National Science Foundation's MRSEC program (DMR-1121262). We are also grateful to the Initiative for Sustainability and Energy at Northwestern (ISEN) for grants to upgrade NUCAPT's capabilities.

References

[1] R.J. Mitchell, M. Preuss, S. Tin, M.C. Hardy, The influence of cooling rate from temperatures above the γ′ solvus on morphology, mismatch and hardness in advanced polycrystalline nickel-base superalloys, Materials Science and Engineering: A 473(1-2) (2008) 158-165.
[2] Y.W. Zhang, Y.H. Shangguan, Research and development in P/M superalloy, Powder metallurgy industry 14 (2004) 30-43.
[3] R.C. Reed, The superalloys, fundamentals and applications, Cambridge University Press, Cambridge, 2006.
[4] M.K. Miller, Contributions of atom probe tomography to the understanding of nickel-based superalloys, Micron 32 (2001) 757-762.
[5] J. Gayda, T.P. Gabb, P.T. Kantzos, The effect of dual microstructure heat treatment on an advanced nickel base disk alloy, Superalloys (2004) 323-329.
[6] J. Mao, K.M. Chang, W.H. Yang, D.U. Furrer, K. Ray, S.P. Vaze, Cooling precipitation and strengthening study in powder metallurgy superalloy Rene88DT, Materials science and Engineering A (2002) 318-329.
[7] M.P. Jackson, R.C. Reed, Heat treatment of UDIMET 720Li, the effect of microstructure on properties, materials science and engineering A 259 (1999) 85-97.
[8] R.C. Reed, The superalloys, fundamentals and applications., Cambridge University Press, Cambridge, 2006.
[9] R.J. Mitchell, M.C. Hardy, M. Preuss, S. Tin, Development of gamma' morphology in PM rotor disc alloys during heat treatment, Superalloys (2004).
[10] G.F. Tian, C.C. Jia, Y. Wen, B.F. Hu, Effect of solution cooling rate on the γ′ precipitation behaviors of a Ni-base PM superalloy, University of science and technology Beijing 15 (2008) 729-734.
[11] J.Y. Hwang, R. Banerjee, J. Tiley, R. Srinivasan, G.B. Viswanathan, H.L. Fraser, Nanoscale Characterization of Elemental Partitioning between Gamma and Gamma Prime Phases in René 88 DT Nickel-Base Superalloy, Metallurgical and Materials Transactions A 40(1) (2008) 24-35.
[12] S.S. Babu, M.K. Miller, J.M. Vitek, S.A. David, Characterization of the microstructure evolution in a nickel base superalloy during continuous cooling conditions, Acta Materialia 49(20) (2001) 4149-4160.
[13] D.N. Seidman, C.K. Sudbrack, K.E. Yoon, The use of 3-D atom-probe tomography to study nickel-based superalloys, JOM 58(12) (2006) 34-39.
[14] J. Gayda, P. Kantzos, J. Miller, Quench crack behavior of nickel-base disk superalloys, Practical Failure Analysis 3(1) (2003) 55-59.
[15] M.C.H. R.J. Mitchell, M. Preuss and S. Tin, Development of gamma ' morphology in PM rotor disc alloys during heat treatment, Superalloys (2004).
[16] A.R.P. Singh, S. Nag, S. Chattopadhyay, Y. Ren, J. Tiley, G.B. Viswanathan, H.L. Fraser, R. Banerjee, Mechanisms related to different generations of γ′ precipitation during continuous cooling of a nickel base superalloy, Acta Materialia 61(1) (2013) 280-293.
[17] A.R.P. Singh, S. Nag, J.Y. Hwang, G.B. Viswanathan, J. Tiley, R. Srinivasan, H.L. Fraser, R. Banerjee, Influence of cooling rate on the development of multiple generations of γ′ precipitates in a commercial nickel base superalloy, Materials Characterization 62(9) (2011) 878-886.
[18] P.M. Sarosi, B. Wang, J.P. Simmons, Y. Wang, M.J. Mills, Formation of multimodal size distributions of γ′ in a nickel-base superalloy during interrupted continuous cooling, Scripta Materialia 57(8) (2007) 767-770.

[19] M.Z. Li, G.F. Tian, private communication, 2016.
[20] M. Zielinska, M. Yavorska, M. Poreba, J. Sieniawski, Thermal properties of cast nickel based superalloys, Archives of Materials Science and Engineering 44(1) (2010) 35-38.
[21] J.G. Speight, Lange's handbook of chemistry, McGraw-Hill New York2005.
[22] R.R. Unocic, On the creep deformation mechanisms of an advanced disc Ni-base superalloy, The Ohio State University, 2008.
[23] J. Coakley, D. Dye, H. Basoalto, Creep and creep modelling of a multimodal nickel-base superalloy, Acta Materialia 59(3) (2011) 854-863.
[24] R.A. MacKay, T.P. Gabb, M.V. Nathal, Microstructure-sensitive creep models for nickel-base superalloy single crystals, Materials Science and Engineering: A 582 (2013) 397-408.
[25] E.F.W. P.R. Bhowal, and E.L. Raymond, Effects of cooling rate and γ′ morphology on creep and stress-rupture properties of a powder metallurgy superalloy, Metallurgical and Materials Transactions A 21A (1990) 1709-1717.
[26] G.B. Viswanathan, P.M. Sarosi, M.F. Henry, D.D. Whitis, W.W. Milligan, M.J. Mills, Investigation of creep deformation mechanisms at intermediate temperatures in René 88 DT, Acta Materialia 53(10) (2005) 3041-3057.
[27] D. Blavette, E. Cadel, B. Deconihout, The Role of the Atom Probe in the Study of Nickel-Based Superalloys, Materials Characterization 44 (2000) 133-157.
[28] T.F. Kelly, M.K. Miller, Atom probe tomography, Review of Scientific Instruments 78(3) (2007).
[29] D.J. Larson, T.J. Prosa, R.M. Ulifig, B.P. Geiser, T.F. Kelly, Local electrode atom probe tomography – a user's guide, Springer Verlag, New York, 2013.
[30] S.S.A. Gerstl, D.N. Seidman, A.A. Gribb, T.F. Kelly, Leap microscopes look at TiAl alloys, Advanced Materials and Processes 162(10) (2004) 31-33.
[31] D.M. Collins, L. Yan, E.A. Marquis, L.D. Connor, J.J. Ciardiello, A.D. Evans, H.J. Stone, Lattice misfit during ageing of a polycrystalline nickel-base superalloy, Acta Materialia 61(20) (2013) 7791-7804.
[32] J.Y. Hwang, S. Nag, A.R.P. Singh, R. Srinivasan, J. Tiley, H.L. Fraser, R. Banerjee, Evolution of the γ/γ′ interface width in a commercial nickel base superalloy studied by three-dimensional atom probe tomography, Scripta Materialia 61(1) (2009) 92-95.
[33] E.Y. Plotnikov, Z. Mao, R.D. Noebe, D.N. Seidman, Temporal evolution of the γ(fcc)/γ′(L12) interfacial width in binary Ni–Al alloys, Scripta Materialia 70 (2014) 51-54.
[34] X.P. Tan, D. Mangelinck, C. Perrin-Pellegrino, L. Rougier, C.A. Gandin, A. Jacot, D. Ponsen, V. Jaquet, Spinodal Decomposition Mechanism of γ′ Precipitation in a Single Crystal Ni-Based Superalloy, Metallurgical and Materials Transactions A 45(11) (2014) 4725-4730.
[35] J. Tiley, G.B. Viswanathan, R. Srinivasan, R. Banerjee, D.M. Dimiduk, H.L. Fraser, Coarsening kinetics of γ′ precipitates in the commercial nickel base Superalloy René 88 DT, Acta Materialia 57(8) (2009) 2538-2549.
[36] F. Vogel, N. Wanderka, Z. Balogh, M. Ibrahim, P. Stender, G. Schmitz, J. Banhart, Mapping the evolution of hierarchical microstructures in a Ni-based superalloy, Nature communications 4 (2013) 2955.
[37] M.Z. Li, B.A. Shollock, P. Bagot, Private communication, 2016.

Highlights

- The γ matrix, secondary γ’ and tertiary γ’ chemical compositions from different cooling rates have been measured and compared;
- Secondary precipitates have ‘shells’ with different composition to the cores has been observed;
- A physical model and thermodynamics have been proposed for γ’ formation;
- Sequential equilibria analysis explaining Al and Ti gradient in secondary γ’;
- The findings can provide information for alloy designs.